

## Article

# Reversible Multi-Mode Optical Modification in Inverse-Opal-Structured $\text{WO}_3$ : $\text{Yb}^{3+}$ , $\text{Er}^{3+}$ Photonic Crystal

Bokun Zhu <sup>1</sup>, Keliang Ruan <sup>1</sup>, Cherkasova Tatiana <sup>2</sup> and Yangke Cun <sup>1,\*</sup>

<sup>1</sup> College of Materials Science and Engineering, Kunming University of Science and Technology, Kunming 650093, China; zbk1101@163.com (B.Z.); 18705811258@163.com (K.R.)

<sup>2</sup> School of Chemistry and Oil and Gas Technology, Kuzbas National Technical University, 650026 Kemerovo, Russia; ctg.htnv@kuzstu.ru

\* Correspondence: cunyangke@kust.edu.cn

**Abstract:** Reversible optical regulation has potential applications in optical anti-counterfeiting, storage, and catalysis. Compared to common power materials, the reverse opal structure has a larger specific surface area and an increased contact area for optical regulation, which is expected to achieve higher regulation rates. However, it is difficult to achieve reversible and repeatable regulation of the luminescent properties of photonic crystals, especially with the current research on the structural collapse of photonic crystals. In this work,  $\text{WO}_3$ :  $\text{Yb}^{3+}$ ,  $\text{Er}^{3+}$  inverse photonic crystals were prepared by the template approach, and reversible multi-mode optical modification was investigated. Upon heat treatment in a reducing atmosphere or air, the color of the photonic crystals can reversibly change from light yellow to dark green, accompanied by changes in absorption and upconversion of luminescence intensity. The stability and fatigue resistance of this reversible optical modification ability were explored through cyclic experiments, providing potential practical applications for photocatalysis, optical information storage, and electrochromism.

**Keywords:** upconversion; inverse opal structure; reversible modulation



**Citation:** Zhu, B.; Ruan, K.; Tatiana, C.; Cun, Y. Reversible Multi-Mode Optical Modification in Inverse-Opal-Structured  $\text{WO}_3$ :  $\text{Yb}^{3+}$ ,  $\text{Er}^{3+}$  Photonic Crystal. *Materials* **2024**, *17*, 2436. <https://doi.org/10.3390/ma17102436>

Received: 4 April 2024

Revised: 27 April 2024

Accepted: 7 May 2024

Published: 18 May 2024



**Copyright:** © 2024 by the authors. Licensee MDPI, Basel, Switzerland. This article is an open access article distributed under the terms and conditions of the Creative Commons Attribution (CC BY) license (<https://creativecommons.org/licenses/by/4.0/>).

## 1. Introduction

Lanthanide-ion-doped inorganic luminescent materials are extensively used in photoelectric fields, including in photocatalysis, optical communication, and optical storage [1] due to the abundant luminescent energy levels of lanthanide ions, which contribute to achieving excellent luminescent performance. Rapid advancement in science and technology has led to an exponential increase in the demand for innovative luminescent materials in the aforementioned application domains [2–5]. The modification of optical performance is a pioneering strategy with significant practical implications and theoretical value. Recently, several common optical performance modulation techniques have emerged, for instance, co-doping a matrix or modifying the concentration of specific ions to disrupt the local symmetry of the crystal field to improve rare earth luminescence [6] and adjusting the doping concentration of rare earth ions to adjust the energy transfer of rare earth ions [7,8]. Additionally, using more complex photonic structures like constructing core-shell structures to govern energy transfer [9,10], using photonic crystals with photonic band gaps for selective luminescence enhancement [11], or using the coupling of surface plasmons and photonic crystal effects to enhance luminescence [12,13].

In the aforementioned techniques, photonic crystal materials have demonstrated distinctive advantages as optical materials because of their well-ordered, three-dimensional, macroscopic, porous structure with interconnected pores, wherein each larger air void corresponds to three small dark regions in the lower layer [14,15]. The structure of photonic crystals is characterized by a periodic arrangement, which gives rise to the presence of photonic bandgaps within this periodicity. By manipulating the lattice parameters and

refractive indices of materials, precise control over the optical properties of photonic crystals can be achieved [16,17]. Leveraging the unique structure of photonic crystals to enhance the interaction between light and materials thereby augments the luminescent properties of materials, offering a compelling approach for modulating the optical characteristics of materials, and further expands their applications in fields such as optical storage and photocatalysis. Cheng Zhu et al. investigated the effect of the photonic bandgap on the luminescence characteristics of  $\text{NaYF}_4:\text{Yb, Tm}@\text{SiO}_2$  photonic crystals [18]. However, it is difficult to achieve reversible and repeatable regulation of the luminescent properties of photonic crystals. Current studies still report the existence of a potential risk of structural collapse during optical modulation, which will significantly impact the reversibility and repeatability in practical applications [19]. Therefore, the development of lanthanide-ion-doped photonic crystals with reversible optical performance poses a crucial challenge.

In the field of photocatalysis, commonly employed metal oxide materials include  $\text{TiO}_2$ ,  $\text{WO}_3$ ,  $\text{ZnO}$ ,  $\text{SnO}_2$ , and niobium oxide nanowires, among other notable examples [20–24]. Through the absorption of light in the near-infrared wavelength range, these materials exhibit upconverted luminescent properties, thereby giving them potential applications in fields such as optical communication, optical storage, biomedicine, and photocatalysis. This study presents the design and fabrication techniques for opal gemstone-structured photonic crystal materials. The optical properties of the prepared  $\text{WO}_3:\text{Yb}^{3+}, \text{Er}^{3+}$  inverse photonic crystals are analyzed and explored through advanced optical testing and characterization techniques, providing crucial experimental evidence for comprehending the mechanism of their upconversion luminescence. Finally, this study explores the reversible modulation of absorption and upconversion luminescence performance, showcasing the technique's potential applications in fields such as optical storage, optical sensors, biomarkers, and photocatalysis. These findings present novel concepts and prospects for photonic crystal materials.

## 2. Materials and Methods

### 2.1. Sample Preparation

#### (1) Preparation of Polystyrene (PS) Opal Templates:

A glass substrate was vertically immersed in a solution of monodisperse polystyrene microspheres with a concentration of 10% using the vertical precipitation method. Polystyrene microspheres then self-assembled on the substrate to form ordered opal templates.

#### (2) Preparation of Precursor Sol:

The precursor solutions  $\text{WO}_3: x \text{ mol}\% \text{Yb}^{3+}, 1 \text{ mol}\% \text{Er}^{3+}$  ( $x = 0.5, 1, 2, 3, 4$ ) were prepared using  $(\text{NH}_4)_6\text{H}_2\text{W}_{12}\text{O}_{40} \cdot x\text{H}_2\text{O}$ ,  $\text{Yb}_2\text{O}_3$ ,  $\text{Er}_2\text{O}_3$ , and  $\text{HNO}_3$  as raw materials. The stoichiometric  $\text{Yb}_2\text{O}_3$  and  $\text{Er}_2\text{O}_3$  were weighted to determine the different doping concentrations of  $\text{Yb}^{3+}$  and  $\text{Er}^{3+}$  ions and then dissolved in hot nitric acid to form  $\text{Er}(\text{NO}_3)_3$  and  $\text{Yb}(\text{NO}_3)_3$ , which are then dissolved in anhydrous ethanol.  $(\text{NH}_4)_6\text{H}_2\text{W}_{12}\text{O}_{40} \cdot x\text{H}_2\text{O}$  was dissolved in deionized water and then added dropwise to an alcohol solution of lanthanide nitrates to obtain a precursor solution.

#### (3) Preparation of Inverse Opal Photonic Crystals:

The appropriate amount of precursor sol was slowly added to the PS opal template, and after complete filling, the PS microspheres were removed by sintering at  $480^\circ\text{C}$  for 3 h to obtain  $\text{WO}_3:\text{Yb}^{3+}, \text{Er}^{3+}$  inverse opal photonic crystals.

The above sample preparation method is shown in Figure 1.

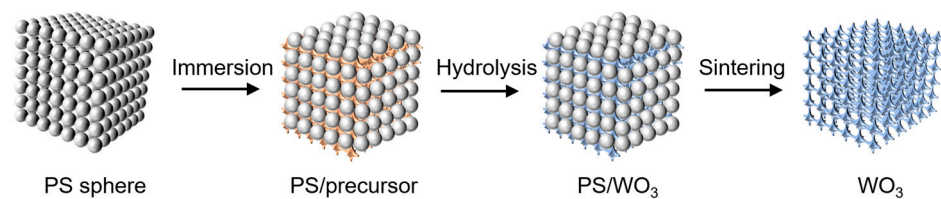


**Figure 1.** The preparation schematic diagram of  $\text{WO}_3: \text{Yb}^{3+}, \text{Er}^{3+}$  inverse opal photonic crystals.

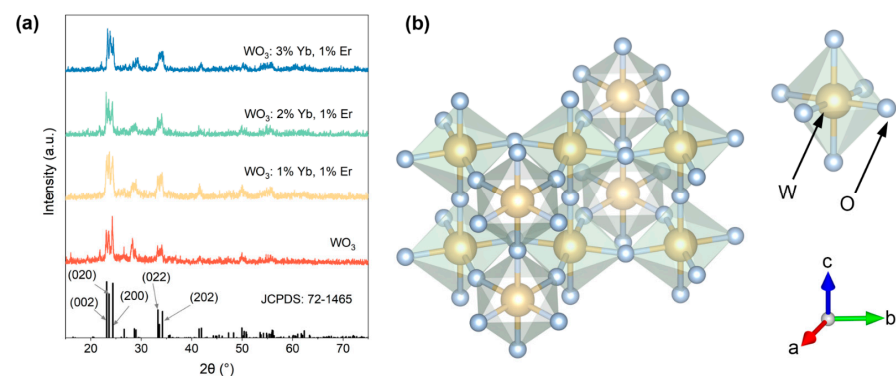
## 2.2. Characterization

The phase analysis of the samples was conducted using an X-ray diffractometer (XRD, D8 ADVANCE, Bruker, Mannheim, Germany). A field emission scanning electron microscope (FESEM, TESCAN MIRA LMS, Brno, Czech Republic) and energy dispersive spectroscopy (EDS) were employed to characterize the morphology and elemental distribution of the samples. X-ray photoelectron spectroscopy (XPS) was performed using a XPS spectrometer (Therma ESCALAB 250XI, Waltham, MA, USA) equipped with a vacuum radiation source emitting 300 W Al K $\alpha$ . The absorption spectra of the samples were examined utilizing a spectrophotometer (HITACHI-U-4100, Tokyo, Japan). Upconversion luminescence measurements were performed employing a fluorescence spectrometer (HITACHI-F-7000, Japan).

## 3. Results and Discussion

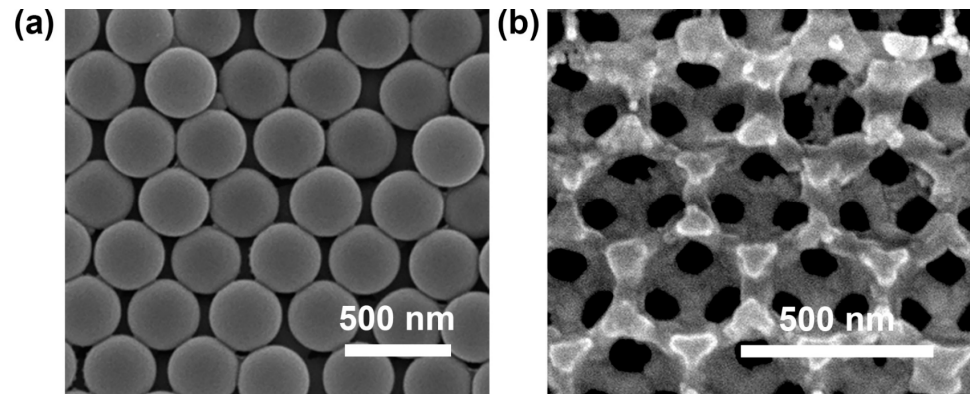
### 3.1. The Phase and Structure of $\text{WO}_3: \text{Yb}^{3+}, \text{Er}^{3+}$ Inverse Photonic Crystals

$\text{WO}_3$  and  $\text{WO}_3: \text{Yb}^{3+}, \text{Er}^{3+}$  inverse photonic crystals with varying doping concentrations of  $\text{Yb}^{3+}$  were synthesized. The XRD patterns were performed on  $\text{WO}_3$  and  $\text{WO}_3: x \text{ mol}\% \text{Yb}^{3+}, 1 \text{ mol}\% \text{Er}^{3+}$  ( $x = 1, 2, 3$ ), as illustrated in Figure 2a. All the XRD diffraction peaks exhibited excellent agreement with the standard PDF card JCPDS: 72-1465 [25] for monoclinic  $\text{WO}_3$ , without any discernible impurity peaks. However, as the doping of lanthanide elements increases, the diffraction peak intensity of  $\text{WO}_3$  increases, which may be due to the doping of lanthanide elements changing the space group of  $\text{WO}_3$  [26]. Figure 2b shows a schematic diagram of the monoclinic phase  $\text{WO}_3$  crystal structure, consisting of an octahedral structure in which the tungsten atom occupies the center and is connected to six oxygen atoms.



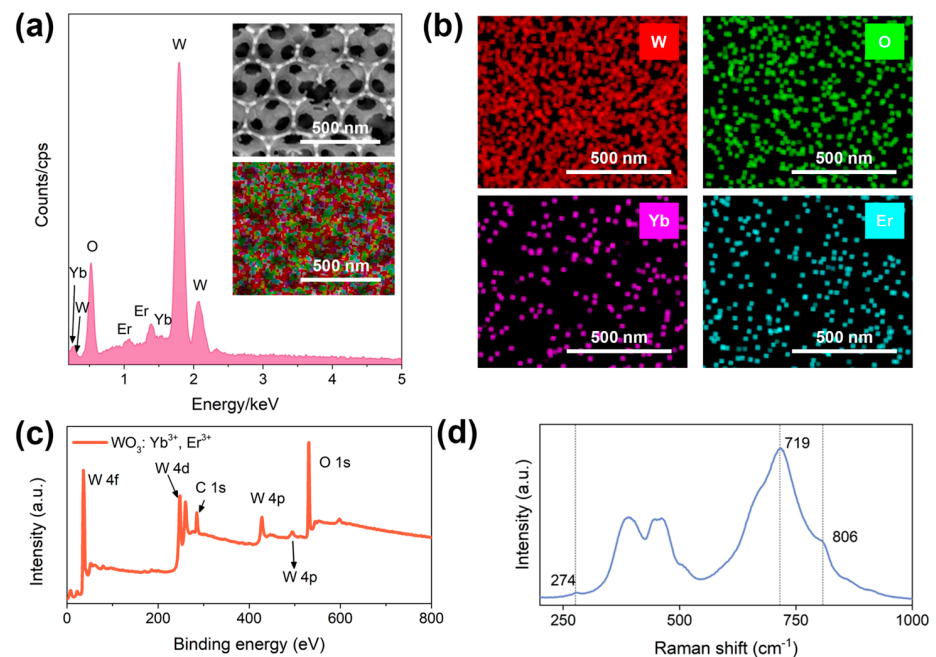
**Figure 2.** (a) XRD patterns of  $\text{WO}_3$  and  $\text{WO}_3: x \text{ mol}\% \text{Yb}^{3+}, 1 \text{ mol}\% \text{Er}^{3+}$  ( $x = 1, 2, 3$ ); (b) schematic diagram of the crystal structure of  $\text{WO}_3$ .

Figure 3a illustrates the polystyrene microsphere opal template obtained through vertical deposition. The SEM image clearly revealed that the uniformly sized polystyrene microspheres formed a densely packed structure with a (111) planarly parallel face-centered cubic (FCC) crystal structure, ensuring a reliable foundation for subsequent photonic crystal synthesis. Furthermore, the surface morphology of the  $\text{WO}_3: 1 \text{ mol}\% \text{Yb}^{3+}, 1 \text{ mol}\% \text{Er}^{3+}$  inverse photonic crystals was analyzed using SEM images in Figure 3b, showing the successful synthesis of an inverted opal structure with a pore size of about 300 nm and a honeycomb-like, three-dimensional, macroporous, ordered structure.



**Figure 3.** (a) The SEM image of the polystyrene microsphere opal template; (b) the SEM image of the  $\text{WO}_3$ : 1 mol%  $\text{Yb}^{3+}$ , 1 mol%  $\text{Er}^{3+}$  inverse photonic crystal.

To further validate the successful doping of  $\text{Yb}^{3+}$  and  $\text{Er}^{3+}$  into the  $\text{WO}_3$  inverse photonic crystal, an EDS analysis was conducted on the  $\text{WO}_3$ :  $\text{Yb}^{3+}$ ,  $\text{Er}^{3+}$  inverse photonic crystal. As shown in Figure 4a, the elements W, O, Yb, and Er were successfully detected in the sample at specific stoichiometric ratios, and elemental analysis showed a uniform distribution of W, O, Yb, and Er elements in  $\text{WO}_3$ , indicating the successful doping of the lanthanide ions to  $\text{Yb}^{3+}$  and  $\text{Er}^{3+}$  into the  $\text{WO}_3$  inverse photonic crystal in Figure 4b. Figure 4c shows the complete XPS spectrum of the  $\text{WO}_3$ :  $\text{Yb}^{3+}$ ,  $\text{Er}^{3+}$  inverse photonic crystal's binding energies, which are further confirmed by comparison with the binding energies provided by the XPS standard spectrum handbook and database. Therefore, the binding energy provides convincing evidence for the successful synthesis of uniformly distributed  $\text{WO}_3$ :  $\text{Yb}^{3+}$ ,  $\text{Er}^{3+}$  inverse photonic crystals. The Raman peaks of the  $\text{WO}_3$ : 1 mol%  $\text{Yb}^{3+}$ , 1 mol%  $\text{Er}^{3+}$  inverse photonic crystal located at 806 and 719  $\text{cm}^{-1}$  are attributed to the stretching vibrations of  $\delta(\text{O-W-O})$ , and the peak at 272  $\text{cm}^{-1}$  belongs to the bending vibration of  $\delta(\text{O-W-O})$ , exhibiting monoclinic structure characteristics [25].



**Figure 4.** (a) The EDS spectrum of the  $\text{WO}_3$ : 1 mol%  $\text{Yb}^{3+}$ , 1 mol%  $\text{Er}^{3+}$  inverse photonic crystal and the corresponding (b) element mapping images; (c) the full XPS spectrum of the  $\text{WO}_3$ : 1 mol%  $\text{Yb}^{3+}$ , 1 mol%  $\text{Er}^{3+}$  inverse photonic crystal; (d) the Raman spectrum of the  $\text{WO}_3$ : 1 mol%  $\text{Yb}^{3+}$ , 1 mol%  $\text{Er}^{3+}$  inverse photonic crystal.

### 3.2. The Optical Performance of $\text{WO}_3: \text{Yb}^{3+}, \text{Er}^{3+}$ Inverse Photonic Crystal

Based on the successful synthesis confirmation of the photonic crystal  $\text{WO}_3: \text{Yb}^{3+}, \text{Er}^{3+}$ , the absorption spectra were measured for both  $\text{WO}_3$  and  $\text{WO}_3: x \text{ mol}\% \text{Yb}^{3+}, 1 \text{ mol}\% \text{Er}^{3+}$  ( $x = 0.5, 2, 3, 4$ ) inverse photonic crystals. As depicted in Figure 5a, the distinct absorption band observed in the range of 500–550 nm for  $\text{WO}_3$  belongs to the bandgap peak of  $\text{WO}_3$  inverse photonic crystals. Doping with lanthanides weakens the peak bandgap due to the decrease in the  $\text{WO}_3$  inverse photonic crystal's structural order. However, with the increase in the  $\text{Yb}^{3+}$  concentration, the absorption ability of the sample in the near-infrared region above 700 nm gradually increase due to the increase in the number of oxygen vacancies in the matrix caused by the lanthanide doping [25]. DFT calculations indicate that the formation of oxygen vacancies in  $\text{WO}_3$  leads to the formation of localized energy levels in the forbidden band, with more W atoms transitioning to lower valence states. The transition of localized energy levels above the Fermi level facilitates a wide range of photoresponses in the visible NIR region [27]. These findings indicate that by incorporating lanthanide ions through doping and adjusting their concentrations, it becomes possible to modulate the optical absorption capability of  $\text{WO}_3$  inverse photonic crystals in the near-infrared region.

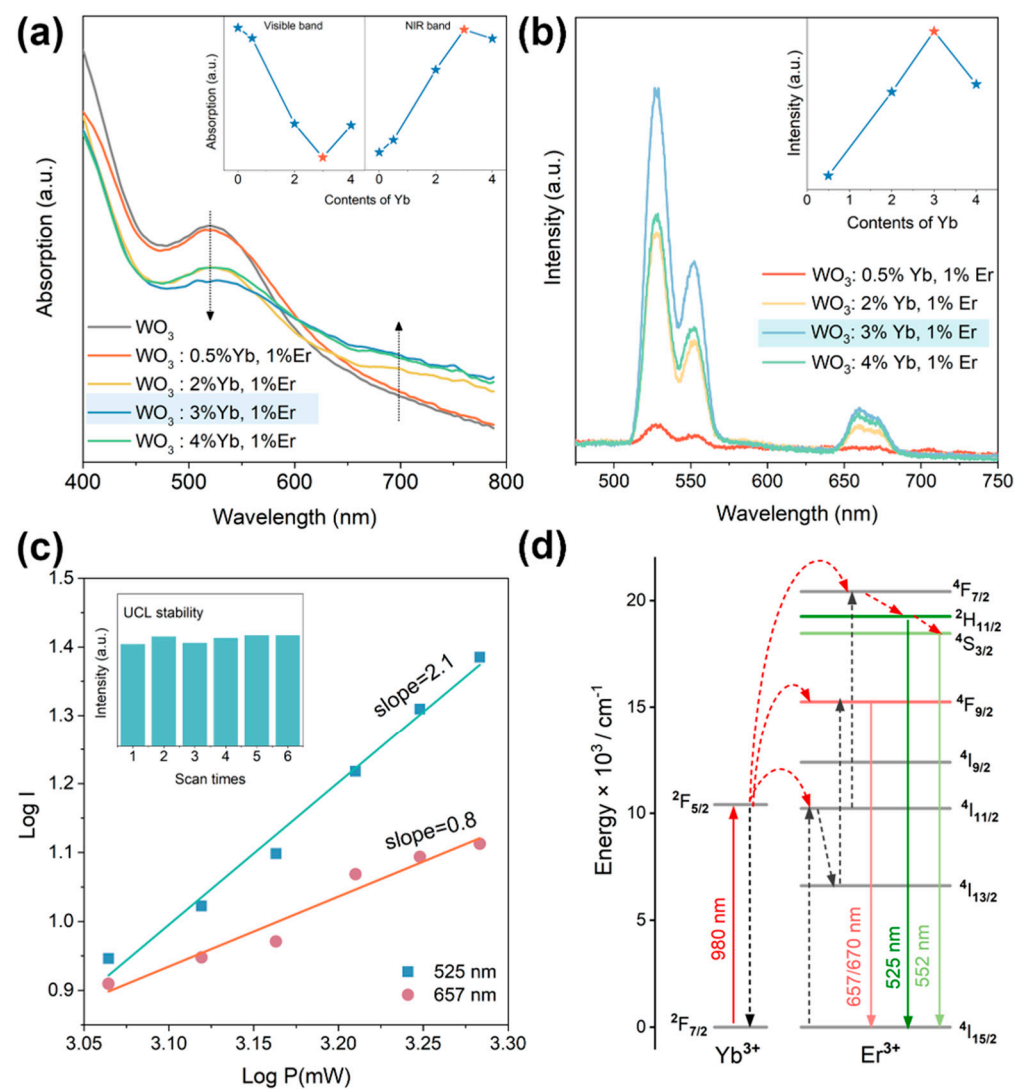


**Figure 5.** (a) Absorption spectra of  $\text{WO}_3$  and  $\text{WO}_3: x \text{ mol}\% \text{Yb}^{3+}, 1 \text{ mol}\% \text{Er}^{3+}$  ( $x = 0.5, 2, 3, 4$ ); (b) the UCL spectra of  $\text{WO}_3: x \text{ mol}\% \text{Yb}^{3+}, 1 \text{ mol}\% \text{Er}^{3+}$  ( $x = 0.5, 2, 3, 4$ ) excited at 980 nm; (c) the UCL stability (inset) and logarithmic plot of UCL intensity of  $\text{WO}_3: 3 \text{ mol}\% \text{Yb}^{3+}, 1 \text{ mol}\% \text{Er}^{3+}$ ; (d) diagram of the UCL mechanism of the  $\text{WO}_3: \text{Yb}^{3+}, \text{Er}^{3+}$  inverse photonic crystal.

The photoluminescence spectra of  $\text{WO}_3: x \text{ mol\% Yb}^{3+}, 1 \text{ mol\% Er}^{3+}$  ( $x = 0.5, 2, 3, 4$ ) inverse photonic crystals excited by a near-infrared 980 nm laser are presented in Figure 5b. As illustrated in Figure 5b, the upconversion luminescence intensity of  $\text{WO}_3: \text{Yb}^{3+}, \text{Er}^{3+}$  inverse photonic crystals is gradually amplified with the increasing doping concentration of  $\text{Yb}^{3+}$  ions under the excitation of a 980 nm laser. However, when the concentration of  $\text{Yb}^{3+}$  reaches 3%, the upconversion luminescence (UCL) intensity becomes saturated and diminishes upon further increases in the  $\text{Yb}^{3+}$  concentration due to the influence of the concentration quenching mechanism [28]. Therefore, the optimal doping concentration of  $\text{Yb}^{3+}$  in the  $\text{WO}_3$  inverse photonic crystal is determined to be 3%. As depicted, when excited by near-infrared light at 980 nm, all samples exhibit green UCL peaks at 525 nm and 552 nm emitted from the  $\text{Er}^{3+} {}^2\text{H}_{11/2}/{}^4\text{S}_{3/2} \rightarrow {}^4\text{I}_{15/2}$  transition, and the red UCL peaks exhibited at 657 nm and 670 nm are generated by the  ${}^4\text{F}_{9/2} \rightarrow {}^4\text{I}_{15/2}$  transitions of  $\text{Er}^{3+}$  [29–31]. In general, the equation  $I = P^n$  can be used to investigate the UCL mechanism, where  $I$ ,  $P$ , and  $n$  are the UCL intensity, the 980 nm laser power, and the number of photons, respectively. Figure 5c shows the red and green UCL intensities of  $\text{WO}_3: 3 \text{ mol\% Yb}^{3+}, 1 \text{ mol\% Er}^{3+}$  as a function of different laser powers. The  $n$  at 525 nm is about 2, and the  $n$  at 657 nm is about 1 because of the saturation effect due to the competition between linear decay and upconversion processes caused by the depletion of intermediate excited states [32].

Figure 5d illustrates the intricate mechanism behind the mesmerizing green and red UCL in  $\text{WO}_3: \text{Yb}^{3+}, \text{Er}^{3+}$ . Under 980 nm excitation, the increase in green UCL emissions levels is mainly realized by the energy transfer process from  $\text{Yb}^{3+}$  to  $\text{Er}^{3+}$ , and the electrons of the  ${}^4\text{F}_{7/2}$  energy level undergo non-radiative relaxation to reach the  ${}^2\text{H}_{11/2}$  and  ${}^4\text{S}_{3/2}$  energy levels and finally transition to the ground state  ${}^4\text{I}_{15/2}$  energy level to excite the green UCL emission. The increase in the  ${}^4\text{F}_{9/2}$  level of UCL emissions mainly comes from electrons at the  ${}^4\text{I}_{11/2}$  level undergoing non-radiative relaxation to the  ${}^4\text{I}_{13/2}$  level and then absorbing the energy of  $\text{Yb}^{3+}$  ions to transition to the  ${}^4\text{F}_{9/2}$  level. The electrons in the final excited state  ${}^4\text{F}_{9/2}$  level transition to the ground state  ${}^4\text{I}_{15/2}$  level, producing red UCL emissions. The results suggest that the UCL properties of the  $\text{WO}_3$  inverse photonic crystal can be modulated by adjusting the doping concentration of lanthanide ions. In conclusion, successful modulation of optical absorption capabilities in the visible and near-infrared regions, as well as the properties of upconversion luminescence of lanthanide-ion-doped inverse photonic crystals, has been achieved through lanthanide ion doping and regulation of the doping concentration, demonstrating potential applications in areas such as photocatalysis and optical storage.

### 3.3. Reversible Optical Modulation in $\text{WO}_3: \text{Yb}^{3+}, \text{Er}^{3+}$ Inverse Photonic Crystal

To further explore the potential applications of  $\text{WO}_3: \text{Yb}^{3+}, \text{Er}^{3+}$  in the field of optics, the obtained  $\text{WO}_3: \text{Yb}^{3+}, \text{Er}^{3+}$  inverse photonic crystal materials were sintered at 600 °C for 3 h in an  $\text{N}_2/\text{H}_2$  atmosphere in a tubular furnace. Remarkably, this treatment resulted in a transformation of the light-yellow samples into a dark green coloration. In order to assess the light absorption capacity after the heat treatment in an  $\text{N}_2/\text{H}_2$  atmosphere, absorption tests were conducted on both the original and heat-treated  $\text{WO}_3: \text{Yb}^{3+}, \text{Er}^{3+}$  inverse photonic crystals, as depicted in Figure 6a. The findings unequivocally demonstrate that heat treatment under an  $\text{N}_2/\text{H}_2$  atmosphere enhances the absorption capability of  $\text{WO}_3: \text{Yb}^{3+}, \text{Er}^{3+}$  inverse photonic crystals for visible and near-infrared light. This phenomenon can be attributed to a substantial increase in oxygen vacancies within the reducing environment, leading to more oxygen vacancies assisting in the accumulation of a large number of electrons and the transition from  $\text{W}^{6+}$  to  $\text{W}^{5+}$ , exhibiting significant absorption promotion, especially in the NIR region, as elucidated by Lu et al.'s research [27]. The increased capacity in absorption ( $\Delta\text{Abs}$ ) can be characterized using Formula (1):

$$\Delta\text{abs} = (\text{Abs}_0 - \text{Abs}_n) / \text{Abs}_0 \times 100\% \quad (1)$$

where  $Abs_0$  and  $Abs_n$  represent the absorption spectral intensity of the  $WO_3: Yb^{3+}, Er^{3+}$  photonic crystal before (light yellow) and after (dark green) heat treatment, respectively. Calculations demonstrate that the  $\Delta Abs$  value is 61.4%, indicating the exceptional absorption modulation capability of  $WO_3: Yb^{3+}, Er^{3+}$  in an  $N_2/H_2$  atmosphere. Additionally, upon subjecting the dark green  $WO_3: Yb^{3+}, Er^{3+}$  photonic crystal to a 1 h heat treatment process in air, it is evident that the sample's color reverts back to its initial light-yellow hue, while the absorption intensity fully regains its original strength; the corresponding bright field photographs are shown in Figure 6a. The electrons in the oxygen vacancy defects return to the valence band through the conduction band and oxidize the valence state of  $W$  to  $W^{6+}$  when exposed to atmospheric conditions, leading to the bleaching of  $WO_3: Yb^{3+}, Er^{3+}$  photonic crystal [33]. The  $WO_3: Yb^{3+}, Er^{3+}$  inverse photonic crystals also provide possibilities for electrochromism, as the principle of electrochromism is also the change in the  $W$  valence state caused by ion insertion. To further investigate the repeatability of the unique reversible color change phenomenon, the  $WO_3: Yb^{3+}, Er^{3+}$  photonic crystal was subjected to repeated cycles of heat treatment under a  $N_2/H_2$  reducing atmosphere and an air atmosphere. The corresponding absorption spectral intensity for each cycle was recorded, as depicted in Figure 6b. The results suggest that through multiple iterations of this process, the amplification and attenuation of the absorption intensity in  $WO_3: Yb^{3+}, Er^{3+}$  photonic crystal can be repeatedly modulated without any degradation. This showcases exceptional reversibility and repeatability in absorption modulation, positioning  $WO_3: Yb^{3+}, Er^{3+}$  photonic crystals as highly promising materials with remarkable economic advantages, fatigue resistance, and damage resilience for practical applications in the field of optics.

Based on the realization of absorption modulation, the UCL properties of  $WO_3: Yb^{3+}, Er^{3+}$  inverse photonic crystals were evaluated by heat treatment in a reducing atmosphere, as depicted in Figure 6c. Following heat treatment in a  $N_2/H_2$  reducing atmosphere for 3 h, the initial sample exhibited a significant reduction in the intense green UCL peak at 525 nm and 552 nm, along with a diminished red upconversion luminescence peak at 657 nm and 670 nm. The corresponding luminescence dark field photographs are shown in Figure 6c. According to existing research, this phenomenon can be attributed to the spectral overlap between the absorption and upconversion emission bands of  $WO_3: Yb^{3+}, Er^{3+}$  inverse photonic crystals, resulting in the quenching of upconversion luminescence [34,35]. The modulation capacity of UCL ( $\Delta UCL$ ) can be quantified using the following Formula (2):

$$\Delta UCL = (UCL_0 - UCL_n) / UCL_0 \times 100\% \quad (2)$$

where  $UCL_0$  and  $UCL_n$  represent the UCL intensities of  $WO_3: Yb^{3+}, Er^{3+}$  inverse photonic crystals before (light yellow) and after (dark green) heat treatment, respectively. Calculations reveal a  $\Delta UCL$  value of 95%, demonstrating the exceptional modulation capability of the UCL properties of  $WO_3: Yb^{3+}, Er^{3+}$  under different heat treatment atmospheres. Compared to powder materials,  $WO_3: Yb^{3+}, Er^{3+}$  inverse photonic crystals have a larger comparative area, which increases their contact area during heat treatment in the  $N_2/H_2$  reducing atmosphere and air atmosphere, resulting in a higher optical modulation rate that is beneficial for applications such as photocatalysis, optical information storage, and electrochromism. Furthermore, as depicted in Figure 6d, this study demonstrates that the quenched UCL properties of  $WO_3: Yb^{3+}, Er^{3+}$  inverse photonic crystals can be effectively restored to their original state through heat treatment in air, enabling a reversible cycle of multiple quenching–restoration events for UCL and thus achieving remarkable luminescent modulation capabilities [36].

By integrating the reversible modulation of absorption properties and UCL properties in  $WO_3: Yb^{3+}, Er^{3+}$  inverse photonic crystals, it is feasible to achieve conditional absorption modulation in the visible and near-infrared regions, as well as adjust emission spectra under near-infrared excitation. This process exhibits reversibility and repeatability, thereby facilitating the application of  $WO_3: Yb^{3+}, Er^{3+}$  inverse photonic crystal materials in fields such as photocatalysis, optical information storage, and electrochromism.

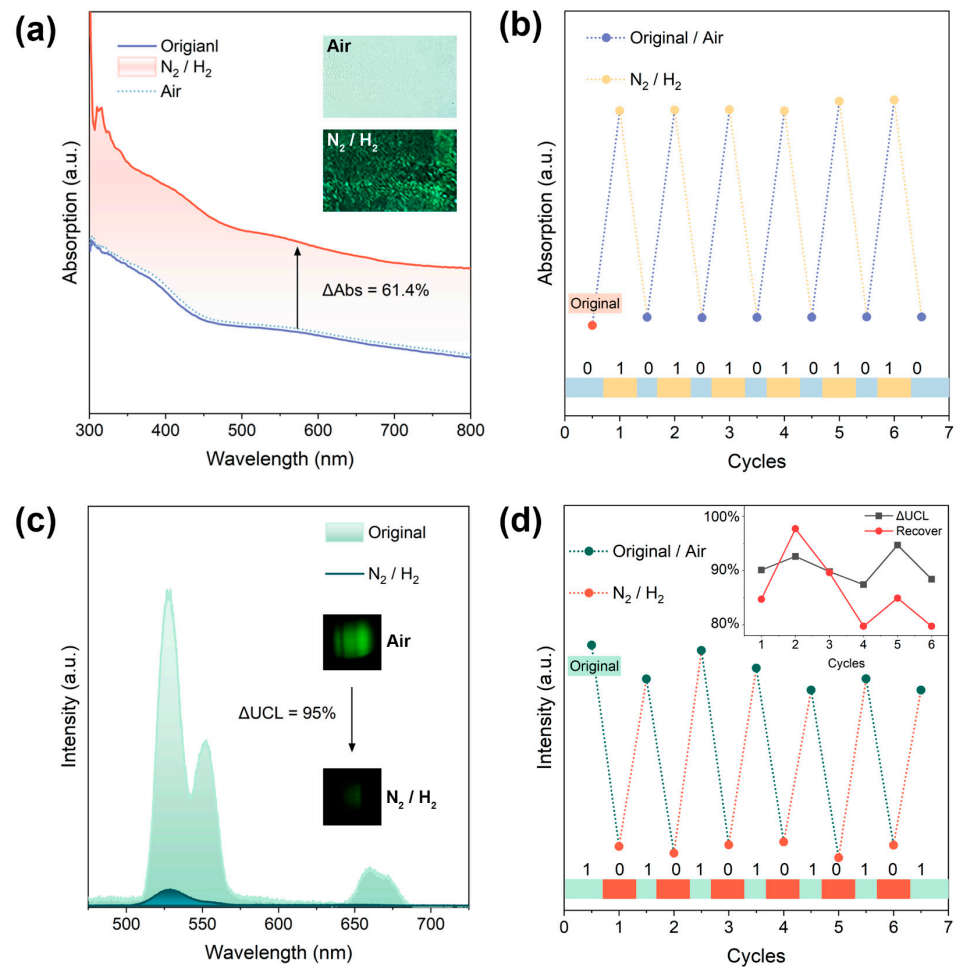


**Figure 6.** (a) Absorption spectra and corresponding photographs of  $\text{WO}_3: \text{Yb}^{3+}, \text{Er}^{3+}$  inverse photonic crystals in pristine state, following heat treatment in an  $\text{N}_2/\text{H}_2$  atmosphere, and subsequent heat treatment in air. (b) Schematic diagram illustrating the absorption cycle of  $\text{WO}_3: \text{Yb}^{3+}, \text{Er}^{3+}$  inverse photonic crystals through alternating heat treatments in  $\text{N}_2/\text{H}_2$  atmosphere and air. (c) The UCL spectra and corresponding photographs of  $\text{WO}_3: \text{Yb}^{3+}, \text{Er}^{3+}$  inverse photonic crystals before and after heat treatment in an  $\text{N}_2/\text{H}_2$  atmosphere and heat treatment in ambient air. (d) The UCL schematic diagram illustrating the cyclic process of alternated heat treatments of  $\text{WO}_3: \text{Yb}^{3+}, \text{Er}^{3+}$  inverse photonic crystals in  $\text{N}_2/\text{H}_2$  atmosphere and air.

#### 4. Conclusions

In this work, the  $\text{WO}_3: \text{Yb}^{3+}, \text{Er}^{3+}$  inverse photonic crystals prepared by the template approach were investigated. The reversible and repeatable UCL and absorption modulation mechanisms were observed under alternating heat treatments in  $\text{N}_2/\text{H}_2$  and air atmospheres, achieving regulation rates of absorption intensity and UCL intensity up to 61.4% and 95% due to the larger specific surface area and increased contact area for optical adjustment of the  $\text{WO}_3: \text{Yb}^{3+}, \text{Er}^{3+}$  inverse photonic crystal structure. The tunable UCL and absorption are attributed to the formation of oxygen vacancies and the transformation of W valence states under different heat treatment atmospheres. This indicates the crystal's potential application prospects in the fields of photocatalysis, optical information storage, and electrochromism, providing guidance for the design and synthesis of new materials for future development.

**Author Contributions:** Y.C. is responsible for writing and revising the paper. B.Z. conducted the experiments with the assistance of Y.C. K.R. provide assistance for investigation and methodology.

C.T. provide assistance for funding acquisition and supervision. All authors have read and agreed to the published version of the manuscript.

**Funding:** This research was funded by the Key Project of the National Natural Science Foundation of China (12204208), the National Natural Science Foundation of the China-Yunnan Joint Fund (U2102215), the Yunnan Fundamental Research Project (grant NO. 202101BE070001-043, 202201AU070119), the Academician Expert Workstation of Yunnan Province (202305AF150099), and the Yunnan Province Major Science and Technology Special Plan (202302AB080005).

**Institutional Review Board Statement:** Not applicable.

**Informed Consent Statement:** Not applicable.

**Data Availability Statement:** Data are contained within the article.

**Conflicts of Interest:** The authors declare no conflicts of interest.

## References

1. Bai, X.; Xu, Z.; Zi, Y.; Xiao, D.; Fu, L.; He, Y.; Zhao, H.; Yang, Z.; Song, Y.; Asif, A.H.; et al. Reversible Fluorescence Modulation and Applications Based on Chromic Effect in Inorganic Rare-earth Luminescent Materials. *Chin. J. Lumin.* **2022**, *43*, 463–477. [[CrossRef](#)]
2. Lv, H.; Du, P.; Luo, L.; Li, W. Negative thermal expansion triggered anomalous thermal upconversion luminescence behaviors in  $\text{Er}^{3+}/\text{Yb}^{3+}$ -codoped  $\text{Y}_2\text{Mo}_3\text{O}_{12}$  microparticles for highly sensitive thermometry. *Mater. Adv.* **2021**, *2*, 2642–2648. [[CrossRef](#)]
3. Nyk, M.; Kumar, R.; Ohulchanskyy, T.Y.; Bergey, E.J.; Prasad, P.N. High contrast in vitro and in vivo photoluminescence bioimaging using near infrared to near infrared up-conversion in  $\text{Tm}^{3+}$  and  $\text{Yb}^{3+}$  doped fluoride nanophosphors. *Nano Lett.* **2008**, *8*, 3834–3838. [[CrossRef](#)]
4. Zheng, B.; Fan, J.; Chen, B.; Qin, X.; Wang, J.; Wang, F.; Deng, R.; Liu, X. Rare-earth doping in nanostructured inorganic materials. *Chem. Rev.* **2022**, *122*, 5519–5603. [[CrossRef](#)]
5. Zhou, Y.; Cheng, Y.; Huang, Q.; Xu, J.; Lin, H.; Wang, Y. Abnormal thermally enhanced upconversion luminescence of lanthanide-doped phosphors: Proposed mechanisms and potential applications. *J. Mater. Chem. C* **2021**, *9*, 2220–2230. [[CrossRef](#)]
6. Song, P.; Qiao, B.; Song, D.; Cao, J.; Shen, Z.; Xu, Z.; Zhao, S.; Wageh, S.; Al-Ghamdi, A. Modifying the crystal field of  $\text{CsPbCl}_3$ :  $\text{Mn}^{2+}$  nanocrystals by co-doping to enhance its red emission by a hundredfold. *ACS Appl. Mater. Interfaces* **2020**, *12*, 30711–30719. [[CrossRef](#)] [[PubMed](#)]
7. Suo, H.; Guo, C.; Li, T. Broad-scope thermometry based on dual-color modulation up-conversion phosphor  $\text{Ba}_5\text{Gd}_8\text{Zn}_4\text{O}_{21}$ :  $\text{Er}^{3+}/\text{Yb}^{3+}$ . *J. Phys. Chem. C* **2016**, *120*, 2914–2924. [[CrossRef](#)]
8. Yang, Z.; Hu, Y.; Chen, L.; Wang, X. Color tuning of  $\text{Ba}_2\text{ZnSi}_2\text{O}_7$ :  $\text{Ce}^{3+}$ ,  $\text{Tb}^{3+}$  phosphor via energy transfer. *J. Lumin.* **2014**, *153*, 412–416. [[CrossRef](#)]
9. Song, Y.; Lu, M.; Mandl, G.A.; Xie, Y.; Sun, G.; Chen, J.; Liu, X.; Capobianco, J.A.; Sun, L. Energy migration control of multimodal emissions in an  $\text{Er}^{3+}$ -doped nanostructure for information encryption and deep-learning decoding. *Angew. Chem.-Int. Ed.* **2021**, *60*, 23790–23796. [[CrossRef](#)]
10. Bednarkiewicz, A.; Prorok, K.; Pawlyta, M.; Strek, W.S. Energy migration up-conversion of  $\text{Tb}^{3+}$  in  $\text{Yb}^{3+}$  and  $\text{Nd}^{3+}$  codoped active-core/active-shell colloidal nanoparticles. *Chem. Mater.* **2016**, *28*, 2295–2300.
11. Yang, Z.; Zhu, K.; Song, Z.; Yu, X.; Zhou, D.; Yin, Z.; Lei, Y.; Qiu, J. Photonic band gap and upconversion emission properties of Yb, Er co-doped lead lanthanum titanate inverse opal photonic crystals. *Appl. Phys. A* **2011**, *103*, 995–999.
12. Shao, B.; Yang, Z.; Wang, Y.; Li, J.; Yang, J.; Qiu, J.; Song, Z. Coupling of Ag nanoparticle with inverse opal photonic crystals as a novel strategy for upconversion emission enhancement of  $\text{NaYF}_4$ :  $\text{Yb}^{3+}$ ,  $\text{Er}^{3+}$  nanoparticles. *ACS Appl. Mater. Interfaces* **2015**, *7*, 25211–25218. [[CrossRef](#)] [[PubMed](#)]
13. Yin, Z.; Li, H.; Xu, W.; Cui, S.; Zhou, D.; Chen, X.; Zhu, Y.; Qin, G.; Song, H. Local field modulation induced three-order upconversion enhancement: Combining surface plasmon effect and photonic crystal effect. *Adv. Mater.* **2016**, *28*, 2518–2525. [[CrossRef](#)] [[PubMed](#)]
14. Armstrong, E.; O'Dwyer, C. Artificial Opal Photonic Crystals and Inverse Opal Structures-Fundamentals and Applications from Optics to Energy Storage. *J. Mater. Chem. C* **2015**, *3*, 6109–6143. [[CrossRef](#)]
15. Chen, Y.; Li, L.; Xu, Q.; Chen, W.; Dong, Y.; Fan, J.; Ma, D. Recent advances in opal/inverted opal photonic crystal photocatalysts. *Sol. RRL* **2021**, *5*, 2000541. [[CrossRef](#)]
16. Butt, M.A.; Khonina, S.N.; Kazanskiy, N.L. Recent advances in photonic crystal optical devices: A review. *Opt. Laser Technol.* **2021**, *142*, 107265. [[CrossRef](#)]
17. Tang, G.-J.; He, X.-T.; Shi, F.-L.; Liu, J.-W.; Chen, X.-D.; Dong, J.-W. Topological photonic crystals: Physics, designs, and applications. *Laser Photonics Rev.* **2022**, *16*, 2100300. [[CrossRef](#)]
18. Zhu, C.; Zhou, W.; Fang, J.; Ni, Y.; Fang, L.; Lu, C.; Xu, Z.; Kang, Z. Improved upconversion efficiency and thermal stability of  $\text{NaYF}_4@SiO_2$  photonic crystal film. *J. Alloys Compd.* **2018**, *741*, 337–347. [[CrossRef](#)]

19. Yang, X.; Jin, H.; Tao, X.; Yao, Y.; Xie, Y.; Lin, S. Photo-Responsive Azobenzene-Containing Inverse Opal Films for Information Security. *Adv. Funct. Mater.* **2023**, *33*, 2304424. [[CrossRef](#)]
20. Akhter, P.; Nawaz, S.; Shafiq, I.; Nazir, A.; Shafique, S.; Jamil, F.; Park, Y.-K.; Hussain, M. Efficient visible light assisted photocatalysis using ZnO/TiO<sub>2</sub> nanocomposites. *Mol. Catal.* **2023**, *535*, 112896. [[CrossRef](#)]
21. Cheng, C.; Amini, A.; Zhu, C.; Xu, Z.; Song, H.; Wang, N. Enhanced photocatalytic performance of TiO<sub>2</sub>-ZnO hybrid nanostructures. *Sci. Rep.* **2014**, *4*, 4181. [[CrossRef](#)] [[PubMed](#)]
22. Rajput, R.B.; Jamble, S.N.; Kale, R.B. A review on TiO<sub>2</sub>/SnO<sub>2</sub> heterostructures as a photocatalyst for the degradation of dyes and organic pollutants. *J. Environ. Manag.* **2022**, *307*, 114533. [[CrossRef](#)]
23. Pligovka, A.; Hoha, A.; Turavets, U.; Poznyak, A.; Zakharau, Y. Formation features, morphology and optical properties of nanostructures via anodizing Al/Nb on Si and glass. *Mater. Today Proc.* **2021**, *37*, A8–A15. [[CrossRef](#)]
24. Pligovka, A.; Zakhlebayaeva, A.; Lazavenka, A. Niobium oxide nanocolumns formed via anodic alumina with modulated pore diameters. *J. Phys. Conf. Ser.* **2018**, *987*, 012006. [[CrossRef](#)]
25. Zhan, Y.; Yang, Z.; Xu, Z.; Hu, Z.; Bai, X.; Ren, Y.; Li, M.; Ullah, A.; Khan, I.; Qiu, J.; et al. Electrochromism induced reversible upconversion luminescence modulation of WO<sub>3</sub>: Yb<sup>3+</sup>, Er<sup>3+</sup> inverse opals for optical storage application. *Chem. Eng. J.* **2020**, *394*, 124967. [[CrossRef](#)]
26. Popov, V.V.; Menushenkov, A.P.; Yastrebtsev, A.A.; Rudakov, S.G.; Ivanov, A.A.; Gaynanov, B.R.; Svetogorov, R.D.; Khramov, E.V.; Zubavichus, Y.V.; Molokova, A.Y.; et al. Multiscale study on the formation and evolution of the crystal and local structures in lanthanide tungstates Ln<sub>2</sub>(WO<sub>4</sub>)<sub>3</sub>. *J. Alloys Compd.* **2022**, *910*, 164922. [[CrossRef](#)]
27. Lu, Y.; Jia, X.; Ma, Z.; Li, Y.; Yue, S.; Liu, X.; Zhang, J. W<sup>5+</sup>-W<sup>5+</sup> pair induced LSPR of W<sub>18</sub>O<sub>49</sub> to sensitize ZnIn<sub>2</sub>S<sub>4</sub> for full-spectrum solar-light-driven photocatalytic hydrogen evolution. *Adv. Funct. Mater.* **2022**, *32*, 2203638. [[CrossRef](#)]
28. Wang, Z.; Meijerink, A. Concentration quenching in upconversion nanocrystals. *J. Phys. Chem. C* **2018**, *122*, 26298–26306. [[CrossRef](#)] [[PubMed](#)]
29. Ma, Y.; Qiu, P.; Xu, D.; Lin, J.; Tang, Y.; Wang, F.; He, X.; Zhou, Z.; Sun, N.; Zhang, X.; et al. Controllable synthesis and upconversion luminescence of NaYF<sub>4</sub>: Yb<sup>3+</sup>, Er<sup>3+</sup> nanocrystals. *Ceram. Int.* **2015**, *41*, S713–S718. [[CrossRef](#)]
30. Yuan, J.; Zheng, G.; Ye, Y.; Chen, Y.; Deng, T.; Xiao, P.; Ye, Y.; Wang, W. Enhanced 1.5 μm emission from Yb<sup>3+</sup>/Er<sup>3+</sup> codoped tungsten tellurite glasses for broadband near-infrared optical fiber amplifiers and tunable fiber lasers. *RSC Adv.* **2021**, *11*, 27992–27999. [[CrossRef](#)]
31. Chung, J.W.; Kwak, M.; Yang, H.K. Improvement of luminescence properties of NaYF<sub>4</sub>:Yb<sup>3+</sup>/Er<sup>3+</sup> upconversion materials by a cross-relaxation mechanism based on co-doped Ho<sup>3+</sup> ion concentrations. *Luminescence* **2021**, *36*, 812–818. [[CrossRef](#)] [[PubMed](#)]
32. Lei, Y.; Song, H.; Yang, L.; Yu, L.; Liu, Z.; Pan, G.; Bai, X.; Fan, L. Upconversion luminescence, intensity saturation effect, and thermal effect in Gd<sub>2</sub>O<sub>3</sub>:Er<sup>3+</sup>, Yb<sup>3+</sup> nanowires. *J. Chem. Phys.* **2005**, *123*, 174710. [[CrossRef](#)] [[PubMed](#)]
33. Ruan, J.; Yang, Z.; Huang, A.; Zhang, H.; Qiu, J.; Song, Z. Thermochromic reaction-induced reversible upconversion emission modulation for switching devices and tunable upconversion emission based on defect engineering of WO<sub>3</sub>: Yb<sup>3+</sup>, Er<sup>3+</sup> phosphor. *ACS Appl. Mater. Interfaces* **2018**, *10*, 14941–14947. [[CrossRef](#)] [[PubMed](#)]
34. Bai, X.; Cun, Y.; Xu, Z.; Zi, Y.; Haider, A.A.; Ullah, A.; Khan, I.; Qiu, J.; Song, Z.; Yang, Z. Multiple anti-counterfeiting and optical storage of reversible dual-mode luminescence modification in photochromic CaWO<sub>4</sub>: Yb<sup>3+</sup>, Er<sup>3+</sup>, Bi<sup>3+</sup> phosphor. *Chem. Eng. J.* **2022**, *429*, 132333. [[CrossRef](#)]
35. Bai, X.; Yang, Z.; Xu, Z.; Cun, Y.; Zi, Y.; Zhao, H.; Song, Y.; He, Y.; Haider, A.A.; Qiu, J.; et al. Optical memory and anti-counterfeiting application based on luminescence reversible modification and color contrast of photochromic phosphor. *Sci. China Mater.* **2023**, *66*, 2408–2417. [[CrossRef](#)]
36. Jimenez, G.L.; Lisiecki, R.; Starzyk, B.; Vazquez-Lopez, C.; Lesniak, M.; Szumera, M.; Szymczak, P.; Kochanowicz, M.; Dorosz, D. Temperature sensing properties of upconverted-emission materials based on a fluorindate glass matrix. *Sens. Actuators A Phys.* **2023**, *357*, 114367. [[CrossRef](#)]

**Disclaimer/Publisher's Note:** The statements, opinions and data contained in all publications are solely those of the individual author(s) and contributor(s) and not of MDPI and/or the editor(s). MDPI and/or the editor(s) disclaim responsibility for any injury to people or property resulting from any ideas, methods, instructions or products referred to in the content.